PAPER

Generation and characterisation of warm dense matter with intense lasers

To cite this article: D Riley 2018 *Plasma Phys. Control. Fusion* **60** 014033

View the article online for updates and enhancements.

Generation and characterisation of warm dense matter with intense lasers

D Riley

Centre for Plasma Physics, School of Mathematics and Physics, Queen's University Belfast, University Road, Belfast BT7 1NN, United Kingdom

E-mail: d.riley@qub.ac.uk

CrossMark

Abstract

In this paper I discuss the subject of warm dense matter (WDM), which, apart from being of academic interest and relevant to inertial fusion capsules, is a subject of importance to those who wish to understand the formation and structure of planetary interiors and other astrophysical bodies. I broadly outline some key properties of WDM and go on to discuss various methods of generating samples in the laboratory using large laser facilities and outline some common techniques of diagnosis. It is not intended as a comprehensive review but rather a brief outline for scientists new to the field and those with an interest but not working in the field directly.

Keywords: warm dense matter, laser drive shocks, dense plasmas, x-ray diagnostics

(Some figures may appear in colour only in the online journal)

Introduction

The study of warm dense matter (WDM) in the laboratory has matured over the last 20 years or so into a well-developed field with many active researchers [e.g. 1–7]. The reason for this is a combination of the exciting and interesting academic challenges inherent and also the important application to understanding the structure and formation of planets and other astrophysical objects, such as brown dwarfs. There have been many scientific questions posed regarding the structure of planets over the last 30 or more years. For example, it has been suggested that the extreme conditions inside planets such as Neptune and Uranus may cause carbon to form into diamond layers [8]. It has been further shown by Nettelmann et al [9] that different models of the interior of Jupiter can be created that predict quite different internal structures and yet both predict gravitational moments and other parameters that agree with observation. The key difference is the equation of state used to describe the relationship between pressure, density and temperature for the hydrogen and helium. Such questions can only be resolved once a firmer understanding of WDM has been established.

We can see, in figure 1, a mapping of WDM conditions in terms of the temperature-pressure space occupied. The challenges faced can be described by reference to some of the key properties of WDM. These include strong inter-particle correlation often expressed through the parameter;

$$\Gamma = \frac{q^2}{akT} ,\qquad(1)$$

where q is the charge on a particle and a is some characteristic distance (in the case of ions, the ion-sphere radius). For ions, in high temperature, low density plasmas such as the solar corona or a tokamak, this parameter is much smaller than unity indicating that the Coulombic interactions can be looked at as a small perturbation on the random thermal motion, albeit a perturbation that leads to rich physics. At the other extreme, in solid matter, values of Γ for ions are well in excess of 100 and the thermal motion represents a perturbation about a fixed lattice position. For WDM, we are often in an intermediate regime where neither Coulomb interaction nor thermal energy are a small perturbation of the other. This presents a challenge in theoretical modelling of WDM.

Another important characteristic is partial degeneracy. For low density classical plasmas, electron degeneracy is not a feature and for cold solids and even liquid metals we can usually approximate that the electrons are in the ground configuration. For WDM we can often have $\mu/kT \sim 1$, where μ is the chemical potential. This means that whilst Pauli blocking will play a role in determining, for example, the electron-ion equilibration time and plasma resistivity, we cannot approximate that all electrons are in the ground state. Finally, we can note that partial ionisation is a key aspect of
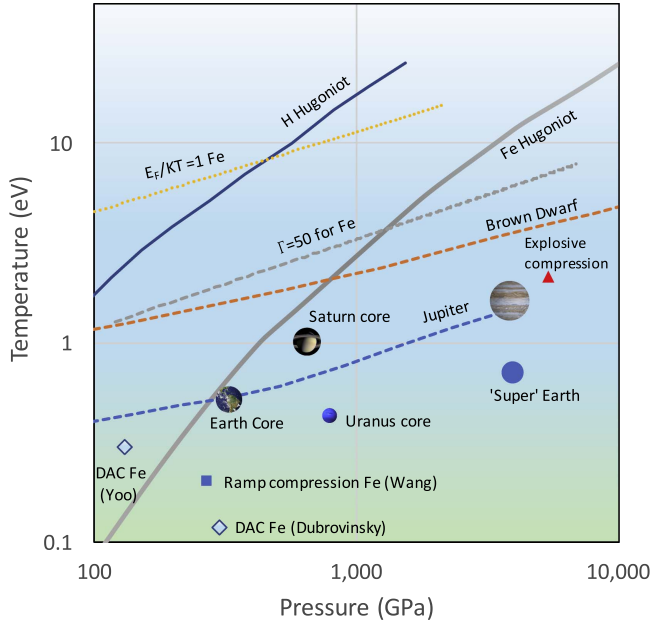
Figure 1. Mapping of the warm dense matter region. The boundaries are a broad guide. We can see the way in which conditions in Jupiter as a function of depth (dashed blue line) pass through the WDM regime as well as conditions in a Brown Dwarf (dashed orange line). We note that static methods of compression and heating such as diamond anvil cells (DAC) only probe the bottom left corner of our regime.

WDM, especially for mid to high-Z elements. This has a significant effect on the microscopic arrangement of ions within the sample as the strong short-range repulsion between bound electron shells might play a part in the inter-ionic potential [10]. In turn, the microscopic structure has profound effects on macroscopic quantities such as the resistivity, compressibility and internal energy of a sample, as we shall discuss further below.

There are some general requirements we can consider in evaluating methods of generating WDM samples. The first of these is the need, in many cases, for a uniform sample. This is important as strong gradients in density and temperature can mask physical effects and make comparison with modelling and theory problematical. Sometimes, we may of course be interested in non-equilibrium situations where heat flows and currents may be generated by gradients, but resolving those gradients in itself becomes a challenge to be met. For this reason, direct heating of a solid by laser-irradiation is generally ruled out as a useful method. Whilst high intensities lead to a hot plasma on the surface and strong electron thermal conduction inwards from the laser-plasma can create WDM conditions in the solid, this is invariably accompanied by very strong density and temperature gradients. The use of very high intensity, short pulse irradiation to create a population of super-thermal electrons that can penetrate a solid and create WDM is a possible exception that will be discussed below.

There are also considerations of timescale. As noted above, static methods such as diamond anvil cells cannot probe most of the WDM regime and we resort to dynamic

methods where a sample is created rapidly and stays in a WDM condition, due to inertia, for long enough for it to be probed. Take, for example, a sample heated to around 10 eV at close to solid density. The speed of expansion can be roughly approximated to the sound speed, which is of order 10^4 ms^{-1} depending on the material. This implies that for millimetre scale targets we can have decompression timescales of order 10^{-8}–10^{-7} s. This is a distinct advantage in terms of probing opportunities. As we shall see, however, such samples present the issue that, for some methods of generation and probing, we would be limited to lower Z materials. This is due to the high opacity for x-rays with higher Z materials and thus smaller samples with consequently faster evolution would be needed.

The timescale is also important from the point of view of equilibration. As noted above, we will sometimes be interested in the process of equilibration in dynamic systems. However, we would often like to compare our data to what may happen inside, for example, a planet where timescales are extremely long. In these cases, when we create a sample, we need to concern ourselves with the rates at which electron-ion exchange of energy, melting and phase changes might occur and compare these to the timescale of our experiment.

In the following sections we will discuss the generation and diagnosis of WDM by a variety of means that use optical lasers, addressing generation and diagnosis together in some cases as some experiments lend themselves to particular diagnostic techniques. We broadly categorise the methods as shock/ramp compression and volumetric heating, both of which can be achieved by a range of means.

Shock or ramp compression

The generation of a shock wave by the sudden application of a high pressure has been discussed and described very well elsewhere [11]. For the purpose of this discussion we will observe that the shock generates a sudden jump in the pressure, density and temperature of a sample. This process is described by the Rankine–Hugoniot equations which consider the conservation of mass, momentum and energy;

$$\rho_0 v_s = \rho v_p$$
$$P_0 + \rho_0 v_s^2 = P + \rho v_p^2$$
$$E_0 + \frac{P_0}{\rho_0} + \frac{v_s^2}{2} = E + \frac{P}{\rho} + \frac{v_p^2}{2}. \qquad (2)$$

There are thus five unknowns, which are the pressure, P, density, ρ, and internal energy, E of the shocked matter and the velocity of the shock, v_s and the particle velocity of the matter after it has been shocked, v_p. If we measure any two of these parameters, we can, in principle, solve for the others. We can see, in figure 1, the so called Hugoniot curves for Fe and Hydrogen taken from the SESAME database [12]. These show how the temperature of the shocked matter is related to the shock pressure. We can also see a point labelled ramp compression. This results from a more gentle compression where pressure is applied in a smooth way rather than a
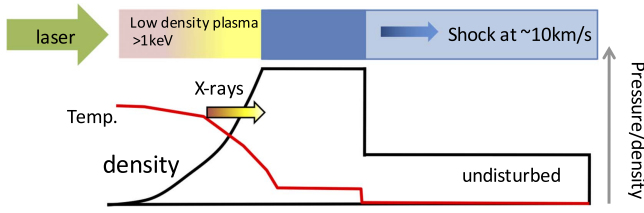
Figure 2. Schematic of a laser driven shock. The incident laser creates a hot plasma on the surface of a solid target. The hot plasma ablates from the surface, exerting a Mbar level pressure that drives a shock into the solid.

sudden jump. The principle on which this is based can be understood by considering that, for an ideal gas, the entropy created by a single shock is given by [see e.g. 11];

$$\Delta S = C_V \ln\left(\frac{PV^\gamma}{P_0 V_0^\gamma}\right). \qquad (3)$$

For strong shocks, it is well known that the maximum compression in an ideal gas is a factor of 4 (given by $(\gamma + 1)/(\gamma - 1)$). If we consider a final shock pressure P, then we can show that by reaching it in a series of shocks of increasing pressure rather than a single jump from P_0 to P, we create less entropy and can, in the limit of specially shaped drive, achieve close to isentropic compression. This permits the exploration of a wider range of conditions away from the shock Hugoniot [e.g. 13, 14], although in many cases we should note that this includes matter below the temperature that we would normally consider as being in the WDM regime.

Directly laser driven shocks

Figure 2 shows a much simplified schematic of laser-shock drive [15–17]. An intense laser incident on a solid surface creates a plasma in which laser light is further absorbed by mechanisms such as inverse bremsstrahlung. Thermal transport into the target creates a dense, high temperature ablation surface where the pressure created drives a shock inwards. There are several scaling laws in the literature that describe the pressure of the shock as a function of the laser intensity and wavelength. For example [17];

$$P(\text{Mbar}) = 8I_{14}^{3/4} \lambda^{-1/2}, \qquad (4)$$

where the laser intensity is in units of $10^{14}\,\text{Wcm}^{-2}$ and the wavelength is in microns. The shock speed depends on the material, being faster for lower density but is generally in the regime of $10\text{s}\,\text{km}\,\text{s}^{-1}$. This implies that for a typical drive duration of 1 ns, a sample of $10\text{s}\,\mu\text{m}$ thickness can be compressed before the pressure source is removed. For direct drive of lasers in this manner, this can create an issue of radiative pre-heating. The keV temperature plasma created in the surface laser–solid interaction will radiate x-rays at several keV. These x-rays can penetrate the solid and heat the material ahead of compression, for example, at 5 keV x-rays have an attenuation length in Al of $20\,\mu\text{m}$. This in turn can alter the Hugoniot so that it is no longer possible to apply the

Rankine–Hugoniot equations without knowledge of the pre-heated conditions.

In addition to radiative pre-heating there can also be electron pre-heating. This can originate in fast electrons created by processes such as filamentation or stimulated Raman scatter in the coronal plasma. The threshold intensity for the latter instability depends of the spatial scale-length of the plasma, L [e.g. see 18]

$$I > \frac{5 \times 10^{16}}{L^{4/3}\lambda^{2/3}}\,\text{W cm}^{-2}, \qquad (5)$$

where L and the wavelength of the laser, λ are in microns. For a keV coronal plasma expanding at sound speed of $2 \times 10^5\,\text{ms}^{-1}$, we expect $L > 200\,\mu\text{m}$ after 1 ns and thus the threshold is below $10^{14}\,\text{W cm}^{-2}$ for $0.527\,\mu\text{m}$ laser light. The issue of pre-heating by supra-thermal electrons in shock experiments was discussed by, amongst others, Trainor and Lee [19].

An important consideration in the generation of such laser-driven shocks is the quality of the focal spot. For some years now optical devices such as random phase plates [20] have been available to counter this problem. There are now several varieties [e.g. 21] of such devices. The basic principle is that the beam is broken into a number of smaller beamlets, for each of which a randomly assigned phase change is introduced, either π or 0. This creates a high frequency interference on the target surface that can be smoothed out via lateral thermal transport in the coronal plasma. The speckle size is typically a few microns and depends on the f-number of focussing and the wavelength. The size of the elements needed is inversely proportional to the size of the focal spot required. This means that for a given f-number and focused intensity, it may be considered that a larger system has some advantages. Firstly, for a larger beam there will be a larger number of elements and so statistical averaging of intensity is more effective. Secondly, with a larger system, a larger focal spot can be used and the ratio of speckle size to focal spot is smaller. Thus, generally higher energy systems (>100 J) are to be preferred for this work. Other methods of beam smoothing such as smoothing by spectral dispersion [22] have also been considered, sometimes in conjunction with a phase plate, although these require modifications to the laser, whilst a phase plate is simply inserted into the beam. An example of a focal spot created with a phase plate is shown in figure 3.

In addition to the focal spot issue, there are other considerations such as the shaping of the laser pulses and the structure of the target. The first of these has been alluded to above in the context of isentropic compression. Prior to the advent of laser pulse shaping technologies, use of multiple beams to create coalescing shocks was considered to obtain higher compression with lower heating [e.g. 23, 24]. Pre-stressed targets have also been used in conjunction with shock waves so that with a different P_0, a different Hugoniot curve is explored. For example [25], compressed helium at up to 60 GPa contained in a diamond anvil cell has been shock compressed with a pulsed laser driving a shock through the diamond into the sample.
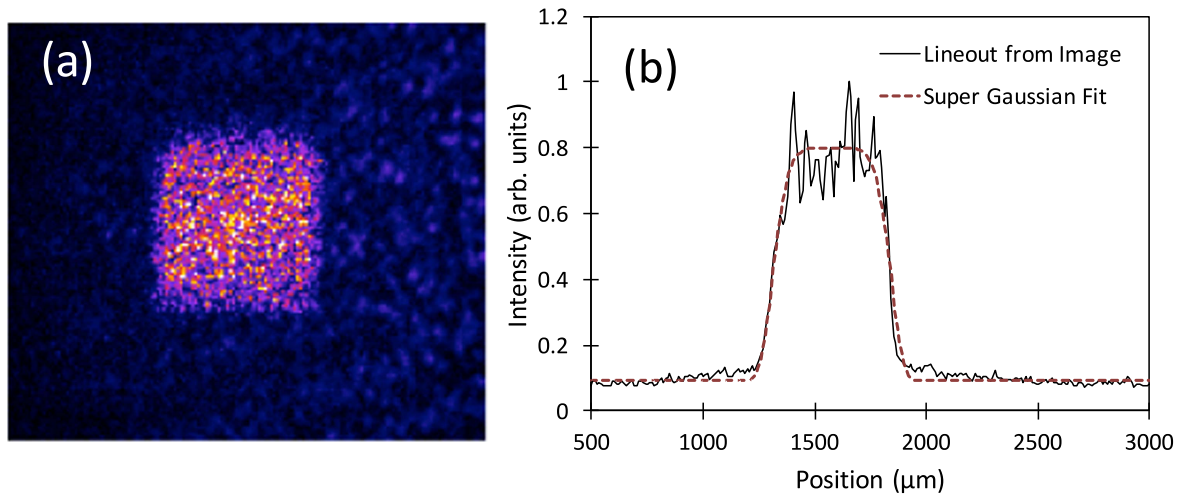
Figure 3. Example of a focal spot shape possible with phase plate technology. (a) Square focal spot with nominal 0.5 mm sides. A low level plateau around the focal spot is due to higher order diffraction and imperfection in manufacture. (b) Lineout average across central part of the spot with a super-Gaussian fit.

Shaping of the shock drive is not just a way to gain a more isentropic compression but, as discussed by Swift and Kraus [26], can be used to maintain a more constant shock driving pressure. As a plasma is created on the surface of the solid, the critical density, at which the laser is absorbed, moves outward and the distance over which thermal conduction needs to deliver energy to the ablation front increases. This generally means a drop in the applied pressure and a rising intensity pulse can help mitigate this factor. We can note, however, that as the scale-length of the coronal plasma increases, the threshold for parametric instabilities such as stimulated Raman scattering becomes lower. The use of an ablator layer, such as CH to absorb the laser light and help form the shock driving pressure has also been discussed [26]. The impedance mismatch between a CH layer and a metal sample leads to a higher shock pressure imposed on the metal than would otherwise be generated by the ablation pressure. This comes at the price of a shorter duration of application peak pressure that comes about as a result of the series of shock reflection and release waves that occur between the plasma-vacuum interface and the CH-metal interface.

Indirectly driven shocks

Intense lasers incident on high Z materials can be efficient sources of x-rays, especially in the sub-keV regime with conversions up to 80% level [27–29]. With sub-keV x-rays the absorption length in a solid can be generally sub-micron and thus they can in principle be used to ablate the surface, exerting an ablation pressure in order to drive a shock. This is often achieved by irradiation of the inside of a gold cavity (hohlraum) with intense laser pulses (see figure 4). The x-ray emission, which can have an equivalent black body temperature of over 200 eV, is allowed to fall onto a shock target which may have an 'ablator' layer, consisting of a low Z material such as CH [13]. In this way, shocks of over 20 Mbar have been generated [30]. In such experiments care has to be taken to ensure that harder x-rays do not penetrate and pre-
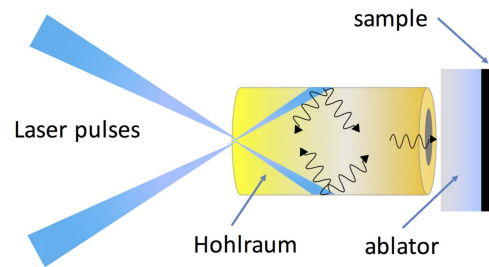

Figure 4. Schematic of a hohlraum target used to create an intense quasi black-body radiation field. Peak radiation is typically about 0.5 keV which has an attenuation length of order 1 micron in CH.

heat the sample. For example, when using Au as the x-ray sources, the M-band radiation is broadly in the 2–4 keV photon energy range and conversion efficiency to M-band from laser energy can easily be several percent [28, 29]. A low Z ablator may need to be of order 100 μm to avoid significant pre-heating of the shocked sample. A key advantage of this method is that non-uniformities in the optical laser profile can be smoothed out by conversion to x-rays and a more uniform shock can be generated. In addition to this, electron pre-heating is mitigated as faster electrons created in the optical laser-plasma interaction may not escape the x-ray generation target.

An alternative is to use a laser irradiated foil as a 'flyer plate'. This flyer plate can be either directly illuminated with a laser beam or indirectly driven with a an intense x-ray source. An example of the latter is [31] in which 25 kJ of laser light in 1 ns drive was focused into a gold hohlraum to create an intense x-ray drive in a that was incident on a foil consisting of a 50 μm polystyrene ablator on a 3 μm Au flyer plate. Collision with a further stepped Au foil generated a shock of Gbar (100 TPa) pressure. The pressure was inferred from the speed of the shock measured by observing the optical emission from the rear of the Au steps as the shock emerged from the rear. Such experiments have the advantage of potentially removing radiative and electron pre-heating but are
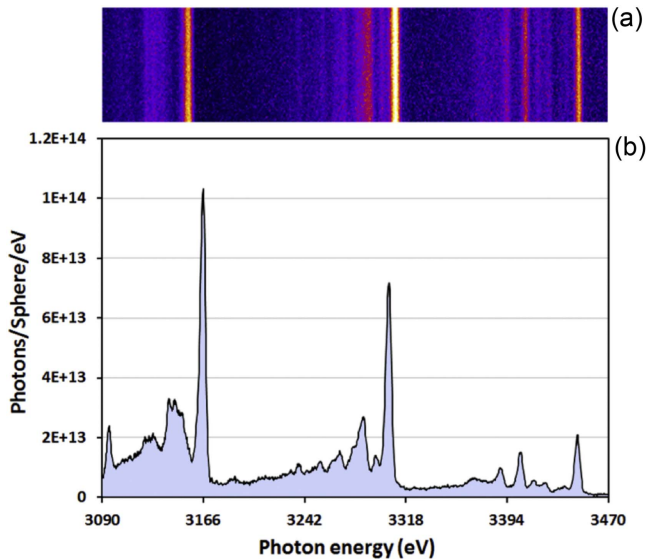
Figure 5. Experimental L-shell emission spectrum from a 50 nm Pd foil irradiated with 527 nm wavelength laser beams with 200 ps FWHM duration. Intensity on target was $\sim 10^{15}$ W cm^{-2} and conversion to L-shell x-rays was estimated at 4%. Similar data can be seen in [34].

susceptible to hydrodynamic instability as the flyer is accelerated and this issue along with any non-uniformity in irradiation can lead to a non-flat impact and thus non-uniform shock drive.

Volumetric heating

X-ray heating

As indicated above, the conversion of laser light to sub-keV x-ray and XUV radiation can be very efficient, reaching 10 s of percent for high Z elements. For volumetric heating we are generally more interested in the harder (>1 keV) x-ray regime as the photons can penetrate a sample and deposit energy uniformly, for example the M-band of Au [32]. Naturally, good uniformity requires a photon absorption length somewhat greater than the sample dimension and this also implies a low efficiency, thus a high available energy is desirable. For mid- Z materials we can create L-shell spectra in the few keV range with several percent conversion of laser light to x-rays [33, 34]. An example spectrum for Pd is shown in figure 5.

An example of the use of volumetric heating with L-shell radiation can be seen in the work of Glenzer *et al* [35] who demonstrated x-ray Thomson scattering (discussed below) using a sub-mm scale Be target heated by L-shell x-rays in the 2.7–3.4 keV range from a Rh shell around the sample. They were able to achieve relatively uniform electron density of over 3×10^{23} cm^{-3} at a temperature of 53 eV. The ion–ion coupling parameter is of order unity. Furthermore, the Fermi energy of the electrons should be 15 eV and thus $E_{\mathrm{F}}/kT \sim 0.3$, illustrating both strong coupling and partial degeneracy; two of the key features of WDM. More recently, Kettle *et al* [36] have used volumetric x-ray heating using Pd L-shell emission
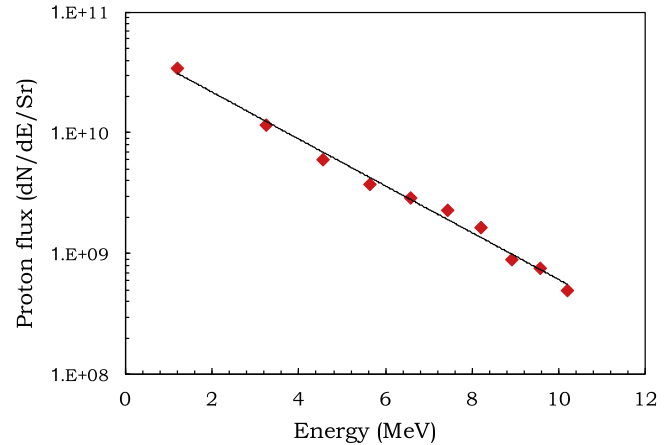

Figure 6. Experimental proton spectrum from the TARANIS laser facility. The 1.053 μm wavelength laser pulse was 7.5 J energy, 1 ps duration focused to about 10 μm focal spot onto a 10 μm thick Au foil. The solid line is a fit to an exponential showing an effective temperature of ~ 2.2 MeV. The latest work in this area has achieved proton energies in excess of 85 MeV [39].

to heat Al to WDM conditions of ~ 1 eV and solid density in order to probe free–free opacity in the XUV radiation. The foils in this case were sub-micron in thickness and thus with a sound speed of ~ 6000 ms^{-1} the decompression time was of order 30–50 ps meaning that rapid heating (<50 ps rise time) and fast probing with sub-ps high harmonic radiation was required. In this case, the ion–ion coupling achieved was of order $\Gamma \sim 50$–80 with $E_{\mathrm{F}}/kT \sim 0.1$–0.15. A further important consideration in this type of experiment is the effect of softer x-rays. If these have a very short absorption length in the solid target then they can result in non-uniform heating as only the outer layers absorb energy. A filter layer, typically a material such as CH is employed as it is relatively transparent to the desired keV heating x-rays whilst reducing the softer x-rays significantly. We are not dealing specifically with x-ray free-electron lasers in this paper, but it is worth noting that a key advantage of such facilities is that they produce an intense beam tuneable to over 10 keV that can be used for uniform volumetric heating [e.g. 37], without an unwanted softer x-ray component.

Proton and fast electron heating

The use of intense short pulse lasers (picosecond and below) to create beams of accelerated protons by mechanisms such as the target-normal-sheath-acceleration (TNSA) mechanism has been well documented for over a decade now [38]. Proton energies up to 10 s of MeV have been routinely achieved. Conversion efficiencies of up to 10% with proton energies in excess of 85 MeV have been reported [39]. The beams typically have some divergence of about a radian and so schemes have been proposed to focus these for WDM creation [40].

A key experimental feature is that there is a spectrum of protons (see example in figure 6). If we consider protons from 5–10 MeV in the heating beam as playing the significant role in heating, then we can readily calculate that even at only 1 mm from the target the temporal dispersion will be

approximately 10 ps. If we consider both the issue of divergence and time of flight, then it is evident that, for now, experiments using these beams to create WDM require a small (mm scale) offset between the intense laser-plasma used to create the beam and the WDM sample. Focusing of the proton beam has been attempted. For example, a hemispherical target has been used, such as described in Patel *et al* [40] to create a WDM sample at 20 eV and solid density. This is well into the WDM regime. However, the sub-mm proximity of the intense laser plasma interaction at $>10^{18}$ W cm^{-2} complicates probing of the sample and it is only from the optical emission from the sample surface that the temperature is diagnosed.

The TNSA mechanism relies on the generation of suprathermal electrons. The efficiency of conversion into such *fast* electrons can be 10 s of percent with temperatures according to the scaling of Beg *et al* [41] given by;

$$T_{\text{hot}} = 100(I\lambda^2)^{1/3} \text{ keV}. \qquad (6)$$

The range of such electrons in solids can be 100 s of microns. As discussed by Bell *et al* [42], the current generated by fast electrons alone would exceed the Alfvén limit and a balancing return current of electrons at lower energy is present. The return current electrons are more collisional and resistive heating of the sample can occur. This process has been used to create WDM, e.g. [43] at temperatures of 10 s eV and solid density, leading to ion–ion coupling parameters of >1 and partial degeneracy. Even more than the proton heating discussed above, a potential limitation of this technique is that the WDM is necessarily in close proximity to a very high temperature non-uniform plasma created by the intense laser interaction and this can create problems with hard x-ray background in diagnostics as well as electromagnetic pulse interference with electronics, which is a known problem with intense laser-plasma experiments.

Diagnostics

Emission spectroscopy is often of limited value in WDM research as the high density and low temperature will combine to make the sample opaque to the wavelengths we would expect from thermally excited emission and so we generally only observe surface emission. We will discuss, below, how this can be used in some diagnostics. There are some exceptions to this case where non-thermally stimulated emission can originate from within the bulk of a sample and analysis can tell us something about density and temperature as well as ionisation. First, we discuss some other key diagnostic methods.

X-ray scattering

X-ray scattering from dense plasmas and WDM has been developed experimentally over the past 20 years [e.g. 35, 44–49] and now sophisticated experiments and analysis can be applied to explore key questions in WDM theory. The basic formulation can be expressed in the following equation;

$$
\begin{aligned}
I(k, \omega) = I_T(k) [\, & (f(k) + q(k))^2 S_{ii}(k, \omega) \\
& + Z_b \int S_b(k, \omega - \omega') S_i(k, \omega') \mathrm{d}\omega' \\
& + Z_f S_{ee}(k, \omega)].
\end{aligned}
\qquad (7)
$$

We can see that there are three contributions to the scattering which are scaled by $I_T(k)$ which is the Thomson scattering cross section as a function of angle, or expressed in this case as a function of scatter wave-vector k. For laser-plasmas, the source is generally unpolarised so this scaling is slightly different than for a polarised source such as an x-ray free electron laser. The first term inside the square bracket is quasi-elastic scattering from bound electrons. The second is bound-free Compton scatter whereby the scattering photon imparts sufficient momentum to a bound electron to cause ionisation. Finally, we have the free-electron scattering. These contributions have been reviewed in detail elsewhere [47, 49]. For the first term $f_i(k)$ is the ionic form factor and $q(k)$ accounts for correlation between free electrons and ions. The term, $S_{ii}(k, \omega)$ is the ion–ion form factor and is connected to the microscopic arrangement of the ions through the pair correlation function $g(r)$. This term is, in principle, dynamic and has a frequency dependence due to motion of the ions. However, most experiments cannot resolve this and we generally expect to measure the related quantity $S_{ii}(k) = \int S_{ii}(k, \omega) \mathrm{d}\omega$. In figure 7(a), we see a scatter cross section as a function of angle for shock compressed Fe, taken with the LCLS x-ray laser operating at 7 keV photon energy. The scattering has been fitted using a hyper-netted chain approach [see e.g. 50] that uses a screened Coulombic potential between the ions supplemented by a short range repulsive term that accounts for the interaction between the shells of bound electrons. An important role of such measurements is that it can connect the microscopic structure of the WDM sample to bulk properties such as the thermal and electrical conductivity as well as compressibility and internal energy. For example [51] the resistivity of a plasma can be expressed as;

$$\rho_e = \frac{m_e^2}{12\pi^3\hbar^3 e^2 n} \int_0^{2k_F} \mathrm{d}k k^3 \, |V_{ei}(qk)|^2 S_{ii}(k). \qquad (8)$$

As we can see, the ion–ion structure factor and thus the pair correlation function $g(r)$ for the sample has a key role.

The second term is the bound-free Compton scatter term [52] and is present when Compton scatter of a photon from a bound electron imparts sufficient recoil energy to an electron to ionise it. The scattered x-ray energies are not simply dependent on the scatter angle as in the usual Compton scatter from free electrons at rest, but show a spectrum that depends on the orbital and the ionisation energy [52]. The final term is the free-electron Thomson scatter. As with optical Thomson scatter this can occur in either the collective or non-collective modes. We see in figure 7(b) a schematic of the collective mode where we see plasmon features either side of the central peak due to elastic scatter. We note that there is an asymmetry in peak intensity governed by the principle of detailed balance
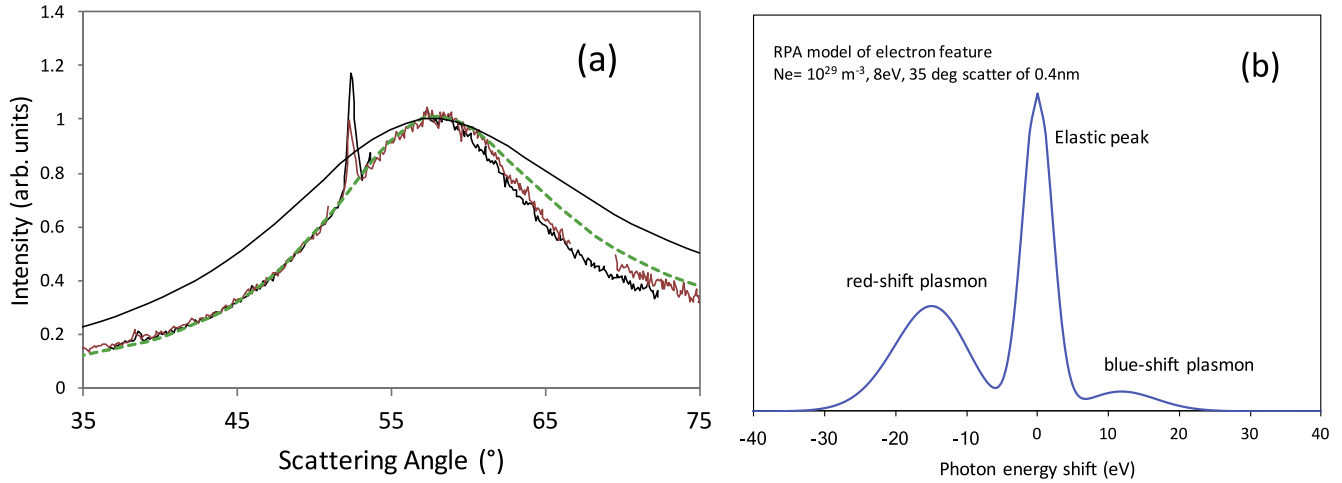
Figure 7. (a) Elastic scatter data as a function of angle for a shock compressed Fe target. The probe photon energy was 7 keV. The black curve is a fit using a simple screened Coulombic potential whilst the green dashed curve is a fit that uses a short range repulsive term of form a/r^4 that accounts for the repulsion between shells of bound electrons. The fit conditions are density of 11.1 g cm^{-3} and T = 1.5 eV. (b) Schematic of the expected spectrum from x-ray Thomson scattering. The plasmon ratio can be linked directly to temperature and the spectral position of the peaks to the electron density. The strength of the elastic peak will depend on the number of bound electrons and so we can see that this is a very powerful diagnostic that can link ionisation state, electron density and temperature.

such that there is a ratio of:

$$I(\omega, k) = I(-\omega, k) \exp\left(-\frac{\hbar\omega}{kT}\right). \qquad (9)$$

This asymmetry is typically not noticeable in optical Thomson scatter as the exponential term is very close to unity. In WDM this is a possible temperature diagnostic that does not depend on the damping of the plasmons or detailed understanding of the plasmon dispersion. Examples of such data can be found in [53, 54].

K-edge and XANES measurements

Since WDM samples are often transparent to x-rays, a key diagnostic is absorption spectroscopy. The existence of edges in the absorption spectra of materials is, of course, well known since the advent of x-ray physics. A key feature for WDM research is that the position of the K-edge, corresponding to the binding of the K-shell electrons, is not fixed but depends on conditions of density and temperature. This dependence arises in simple terms from three factors. The first is continuum lowering or ionisation potential depression (IPD) [e.g. 55] through which the energy levels of bound electrons are raised by interaction with the ambient plasma electric micro-field. This tends to shift the edge position to lower energy. The second term is the shift due to ionisation as a result of the elevated temperature and compression of WDM. This tends to move the edge back to higher energy. Finally, there is the change in degeneracy. Pauli blocking causes the effective edge position to be at a higher energy than would otherwise be the case, this term can shift to either higher or lower energy depending on the temperature and density reached. In the first experimental work using this diagnostic for WDM, Bradley *et al* [56] estimated a shift of -3.7 eV for a KCl sample that was estimated to be at 6.2 gcm^{-3} and 19 eV. This, however, was predicted to be comprised of a continuum lowering of -45.2 eV, an

ionisation shift of $+47.6$ eV and a change due to degeneracy of -6.2 eV. This illustrates a challenge of this diagnostic in that a small net shift is seen and relatively small changes in theory of IPD or estimates of the ionisation can have a large proportional effect on the final result. This issue of IPD is currently a field of renewed interest since recent experimental data from x-ray laser facilities and large laser facilities disagree on which model is appropriate [see 57 and references within].

A more detailed analysis of the edge that looks at oscillations in absorption close to the edge as well as the position can be carried out. These techniques are called EXAFS (extended x-ray absorption fine structure) or XANES (x-ray absorption near edge structure) depending on how far from the edge we are working. The oscillations in absorption coefficient near an edge are caused by quantum mechanical interference. As an electron is ionised in the absorption process, the wave-function of the free state can scatter off nearby ions or atoms and cause oscillations in the final state amplitude that leads to structure in the absorption spectrum. This structure in turn is linked to the microscopic arrangement of the ions. The EXAFS technique has been used in shock compressed samples [58] to look at a region relatively far (~100 eV) from the edge. The density can be deduced from the position of the ion–ion correlation peaks and the temperature will have an effect on the depth of the oscillations, which will smooth out at high temperature. The XANES technique typically looks closer to the edge. The ejected electron has lower energy and multiple scattering from nearby atoms is important. This technique, like EXAFS, is well known in solid state physics but has also been applied to WDM [e.g. 59].

An important experimental detail for any of the absorption techniques is the need for a smooth backlight spectrum. This is needed to see the fine structure easily. Typically, a higher Z target is used where arrays of unresolved transitions
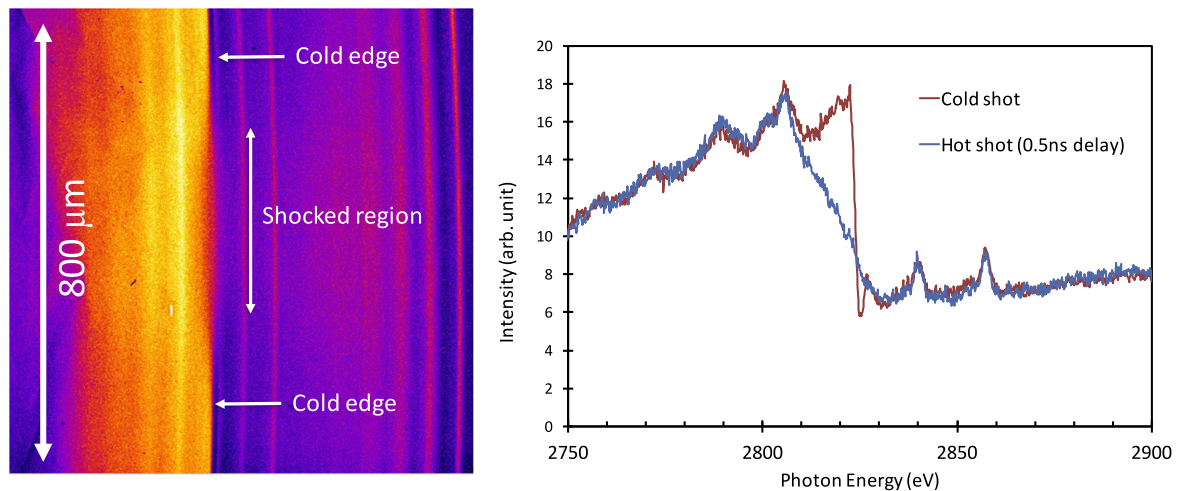
Figure 8. This data shows a comparison of the transmission spectrum for a cold chlorinated plastic target and a shock compressed target. A bismuth back-lighter source was used. We can see that there is good reproducibility in the spectral features of the Bi and there is a clear shift and broadening of the edge. The raw data on the left shows how the small size of the source was used to project through the target with spatial resolution, allowing comparison of the cold and compressed regions directly on each shot. The spatial scale refers to distance across the target sample.

form bands of emission, commonly the M-band of transition between the $n = 4$ to $n = 3$ levels is used. Figure 8 shows an example where Bi has been used to form a K-edge in a shock compressed chlorinated plastic target. In [58] a uranium back-lighter was used as it produces a very smooth N-band spectrum in the required range around the Al K-edge.

Optical pyrometry measurements

As can be seen from the shock Hugoniot curves in figure 1, when a Mbar (100 GPa) shock is used to compress a sample, temperatures of well over 1000 K can be generated. This leads to significant emission in the optical regime, which can be viewed through a transparent sample but also as the shock exits the rear of an opaque sample. This has been used [e.g. 31] to measure shock speeds, in particular by use of stepped target with a known step height.

In addition to the shock break-out time, the optical emission has been used to estimate the temperature. In a transparent medium such as quartz or glass, the emission can be measured before the shock has broken out. In these cases, care has to be taken to understand the optical transmission of the material ahead of the shock. At the high density of the compressed sample, the emission is generally almost black-body in nature and can be used to either measure an emission temperature, from the time resolved absolute level of emission [60] or a spectral temperature by fitting to a grey-body curve. This technique is usually called streaked optical pyrometry (SOP). A detailed discussion of the system implemented at the Omega laser facility is found in [60].

For non-transparent targets there are two options. One is to simply measure the emission as the shock exits the target. This means that there is rapid decompression of the sample as the release wave moves back into the target. The alternative is to use a transparent window. This means that the sample remains at high density as the shock is transmitted into the window material and partially reflected back into the sample.

Window materials such as LiF have been shown to remain transparent at 250 GPa. The quality of the interface and thermal conduction into the window are also key parameters to be considered. As with transparent targets, the optical transmission of the window as it is compressed also needs to be understood to correctly interpret the data. An alternative to a stepped target is to use a timing fiducial laser on an optical streak camera and compare this to the onset of rear surface emission as was also done in [31]. For cases where the optical emission from the rear may be weak, we can consider VISAR as discussed in the next section.

VISAR

An important shock diagnostic commonly run alongside SOP is VISAR, [e.g. 61, 62 and references within] which is an interferometric technique that uses a probe laser to monitor the motion of a surface, such as the rear of the target when a shock breaks out. Details of a design can be found in [61]. The basics are that a beam reflected from the target rear surface is collected and directed into an interferometer. By placing an étalon in one arm of the interferometer but adjusting the path, so that the effective optical path before recombination is the same, then an interference pattern can be formed without stringent coherence requirements that would necessitate a mirror like target and yet the arms sample the reflected surface at different times. The interference pattern is imaged onto the cathode of an optical streak camera, giving spatial resolution across a line on the target surface as well as temporal resolution. If the target remains stationary then so do the fringes created. However, once the rear side accelerates, there is a shift in the fringes. If the surface velocity becomes steady, there is no further shift in fringes. Analysis of the fringe shift can be used to extract the velocity history of the surface [61]. It is common to employ two systems with different fringe sensitivities (different étalon thicknesses) so that if shifts greater than a single fringe width occur, then a unique
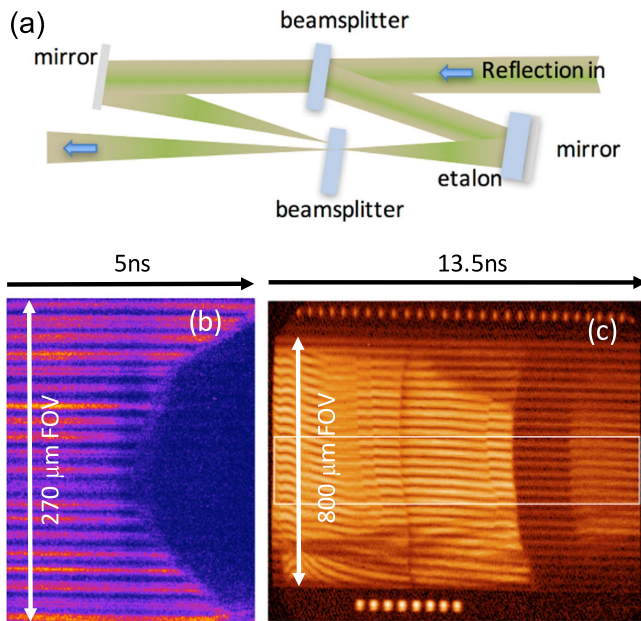
(a)

Figure 9 (a) Schematic of the interferometer at the heart of a VISAR system. (b) Example of VISAR data showing break-out from a laser-shocked Al foil. The focal spot size was 100 μm and we can see the delayed break-out of the shock outside this central zone. The fringes disappear as the shock break out and the surface forms a highly absorbing plasma. (c) Data taken for shock break-out experiment on the Omega laser facility, with a complex layered target consisting of a CH ablator coated onto a quartz pusher with an aerogel foam target on top of that followed by a LiF window [62]. The details of the experiment can be found in [62] and references therein. Image courtesy of K Falk and colleagues.

Figure 10. Ti K-α spectrum from a target irradiated with a sub-picosecond 1.053 μm wavelength pulse at $>10^{18}$ W cm^{-2}. Similar data can be found in [60]. The fit curves are from the SCRAM code [see 43] for different assumed background temperatures. A mixture of regions at different temperatures must contribute to the final spectrum to get the correct ratio of the K-α doublet and the shorter wavelength contribution.

solution can be found by comparing the two systems. In figure 9(b) we see what happens when a shock breaks out from the rear of a simple opaque target. The rear surface rapidly decompresses as a low density plasma/vapour that strongly absorbs the probe and the fringes disappear. For targets with windows and transparent materials we can get more complex data as in figure 9(c) which comes from an experiment in which a shock is driven through a low density aerogel foam. The laser is first incident on a CH ablator layer which is coated onto a quartz pusher. The aerogel is on top of the quartz and this is covered with a LiF window. In the data we can observe several features showing fringe shifts that occur at interfaces where the shock impedance is changing. More details of the experiment can be found in [62].

Emission spectroscopy

Although we have stated above that emission spectroscopy is of limited value, there are occasions when it can be used. For example, we have discussed the fact that fast electron heating can be used to create bulk heating of a solid due to the return current. During this process, the fast electrons can collisionally ionize the inner-shell electrons of the sample. The subsequent K-α emission will come from a range of ionisation states depending on the temperature in the sample [43]. We should also acknowledge that, by its nature, this diagnostic is time integrating as the K-α emission will occur as soon as the
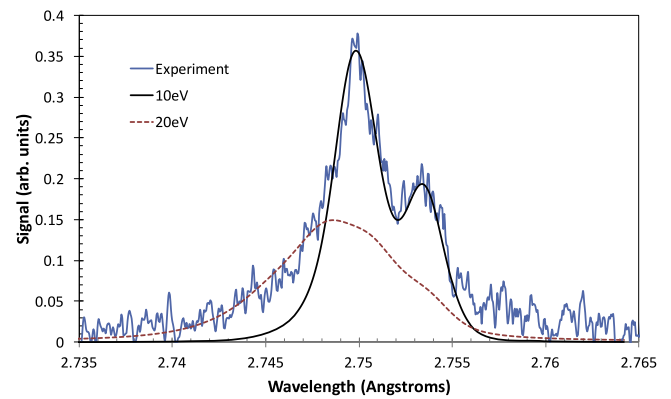
fast electrons penetrate the sample. The K-α lines from adjacent ionisation stages are close in energy and high resolution spectroscopy with $E/\Delta E > 2000$ is desirable. In addition, since we are at high density and Stark broadening may broaden the lines into each other, detailed modelling [43] capability is used to extract the information on plasma conditions.

We see, in figure 10, an example from a Ti sample. The foil is irradiated at $>10^{18}$ W cm^{-2} and subsequent analysis [63] suggested fast electrons generated via a resonance absorption process with temperatures of order 50–100 keV. Analysis of the K-α spectrum created by the fast electrons suggested an ionisation spread consistent with a background temperature of up to 20 eV. Even with spatially and spectrally resolving crystals, the small size of the plasma created makes it difficult to separate out contributions from regions under different conditions. In this case, the spectrum was best fitted by assuming emission coming also from a cold portion of the foil.

As a final example, we can note that, in a recent experiment, fast electrons and shock compression were combined to investigate the issue of IPD [64]. Laser driven shock compression with nanosecond pulses was used to create a high density sample at a few electron volts temperature. In order to stimulate x-ray emission that would originate from the bulk of the sample, an intense short pulse beam was used to create fast electron population that heated the sample to over 500 eV leading to x-ray emission from He-like Al ions. Stark broadening of these lines was used to infer the density and this could be compared to the series cut-off due to the IPD.

Summary

In this paper, I have discussed several methods of creating WDM with intense lasers, from picosecond to nanosecond duration. I have also outlined several of the common diagnostic methods for WDM. Some key factors are the

uniformity and lifetime of the sample as well as the accessibility to probing. There have been many scientists involved in the development of this field, not all of whom have been referenced in this paper. A much wider ranging discussion, in addition to more extensive referencing, would take in the creation of WDM with explosives, Z-pinches, large ion-beam facilities and the relatively new x-ray free electron facilities.

ORCID iDs

D Riley ![ORCID] https://orcid.org/0000-0002-6212-3212

References

[1] Lee R W et al 2003 J. Opt. Soc. Am. B **20** 770
[2] Koenig M et al 2005 Plasma Phys. Contr. Fusion **47** B441
[3] Gaziani F et al (ed) 2014 Frontiers and Challenges Warm Dense Matter (Berlin: Springer)
[4] More R et al 2006 J.Quant. Spectrosc. Radiat.Transfer **99** 409
[5] Nettelmann N, Redmer R and Blaschke D 2008 Phys. Part. Nucl. **39** 1122
[6] Ng A, Ao T, Perrot F, Dharma-Wardana M W C and Foord M E 2005 Laser Part. Beams **23** 527
[7] Renaudin P et al 2003 Phys. Rev. Lett. **91** 075002
[8] Ross M 1981 Nature **292** 435
[9] Nettelmann N et al 2008 Astrophys. J. **683** 1217
[10] Fletcher L B et al 2015 Nat. Photon. **9** 274
[11] Zel'dovich Y B and Razier Y P 2002 Physics of Shock Waves and High-Temperature Hydrodynamic Phenomena (New York: Dover)
[12] Lyon S P and Johnson J D 1992 SESAME: The Los Alamos national laboratory equation of state database LANL Technical Report LA-UR-92-3407 Los Alamos National Laboratory, Los Alamos, NM
[13] Wang J et al 2013 J. Appl. Phys. **114** 023513
[14] Koenig M et al 2010 High Energy Density Phys. **6** 210
[15] Trainor R J et al 1979 Phys. Rev. Lett. **42** 1154
[16] van Kessel C G M and Sigel R 1974 Phys. Rev. Lett. **33** 1020
[17] Thompson P C et al 1981 J. Phys. D **14** 1215
[18] Campbell E M 1992 Phys. Fluids B **4** 3781
[19] Trainor R J and Lee Y T 1982 Phys. Fluids **25** 1898
[20] Kato Y et al 1984 Phys. Rev. Lett. **53** 1057
[21] Pepler D A et al 1995 Diffractive and holographic optics technology II Proc. SPIE **2404** 258
[22] Skupsky S, Short R W, Kessler T, Craxton R S, Letzring S and Soures J M 1989 J. Appl. Phys. **66** 3456
[23] Jackel S, Salzmann D, Krumbein A and Eliezer S 1983 Phys. Fluids **26** 318
[24] Riley D, Willi O, Rose S J and Afshar-Rad T 1989 Europhys. Lett. **10** 135
[25] Eggert J H et al 2009 AIP Conf. Proc. **1161** 26
[26] Swift D C and Kraus R G 2008 Phys. Rev. E **77** 066402
[27] Mochizuki T et al 1986 Phys. Rev. A **33** 525
[28] Goldstone P et al 1987 Phys. Rev. Lett. **59** 56
[29] Kania D R et al 1992 Phys. Rev. A **46** 7853
[30] Löwer T et al 1994 Phys. Rev. Lett. **72** 3186
[31] Cauble R et al 1993 Phys. Rev. Lett. **70** 2102
[32] Perry T S et al 1998 Phys. Rev. E **58** 3739
[33] Phillion D W and Hailey C J 1986 Phys. Rev. A **34** 4886
[34] Kettle B et al 2015 J. Phys. B **48** 224002
[35] Glenzer S H et al 2003 Phys. Rev. Lett. **90** 175002
[36] Kettle B et al 2016 Phys. Rev. E **94** 023203
[37] Levy A et al 2015 Phys. Plasmas **22** 030703
[38] Snavely R A et al 2000 Phys. Rev. Lett. **85** 2945
[39] Wagner F et al 2016 Phys. Rev. Lett. **116** 2005202
[40] Patel P K et al 2003 Phys. Rev. Lett. **91** 125004
[41] Beg F N et al 1997 Phys. Plasmas **4** 447
[42] Bell A R et al 1997 Plasma Phys. Control. Fusion **39** 653
[43] Hansen S B et al 2005 Phys. Rev. E **72** 036408
[44] Woolsey N C, Riley D and Nardi E 1998 Rev. Sci. Instr. **69** 418–24
[45] Riley D et al 2000 Phys. Rev. Lett. **84** 1704–7
[46] Ma T et al 2013 Phys. Rev. Lett. **110** 065001
[47] Glenzer S H and Redmer R 2009 Rev. Mod. Phys. **81** 1625
[48] Gregori G et al 2003 Phys. Rev. E **67** 026412
[49] Gregori G et al 2004 Phys. Plasmas **11** 2754
[50] Wünsch K, Vorberger J and Gericke D O 2009 Phys. Rev. E **79** 010201(R)
[51] Ichimaru S 1982 Rev. Mod. Phys. **54** 1017
[52] Williams B (ed) 1977 Compton Scattering (New York: McGraw Hill)
[53] Glenzer S H et al 2007 Phys. Rev. Lett. **98** 065002
[54] Neumayer P et al 2010 Phys. Rev. Lett. **105** 075003
[55] Stewart J C and Pyatt K D 1966 Astrophys. J. **144** 1203
[56] Bradley D K et al 1987 Phys. Rev. Lett. **59** 2995
[57] Crowley B J B 2014 High Energy Density Phys. **13** 13
[58] Hall T A et al 1988 Phys. Rev. Lett. **60** 2034
[59] Lévy A et al 2009 Plasma Phys. Control. Fusion **51** 124021
[60] Miller J E et al 2007 Rev. Sci. Instrum. **78** 034903
[61] Celliers P M et al 2004 Rev. Sci. Instrum. **75** 4916
[62] Falk K et al 2014 Phys. Rev. E **90** 033107
[63] Makita M et al 2014 Phys. Plasmas **21** 023113
[64] Hoarty D et al 2013 Phys. Rev. Lett. **110** 265003